JOURNAL OF PROPULSION AND POWER
Vol. 24, No. 6, November–December 2008

Characteristics of Gliding Arc and Its Application in Combustion Enhancement

Alexander Fridman,* Alexander Gutsol,† and Shailesh Gangoli‡
Drexel University, Philadelphia, Pennsylvania 19104
and
Yiguang Ju§ and Timothy Ombrello¶
Princeton University, Princeton, New Jersey 08544

DOI: 10.2514/1.24795

A novel magnetically stabilized gliding arc reactor coupled with a counterflow burner was developed to study nonthermal plasma enhancement of ignition and extinction phenomena. The results showed that the new coupled plasma-flame system provides a well-defined platform for understanding of the basic mechanism of the plasma-flame interaction. It was shown that with a plasma discharge of the airstream, up to a 220% increase in the extinction strain rate was possible at low power inputs for air and methane diluted with nitrogen. Measurements of temperature profiles via planar Rayleigh scattering thermometry and OH number density profiles via planar laser-induced fluorescence (calibrated with absorption) were taken to quantify various effects. Detailed numerical simulations at elevated air temperatures and radical addition were performed for comparison with experimentally obtained results. Results of the extinction experiments initially suggested that the enhancement effect was predominantly thermal for our particular setup of experiments. However, in ignition experiments specifically for hydrogen, temperature measurements conducted for hydrogen–air mixtures suggested the contribution of active species to justify the extent of the enhancement effect. Further comparison with numerical simulations also provides an insight into the participation of species other than radicals in the enhancement effect.

Nomenclature

a	=	strain rate of the counterflow flame
B	=	magnetic field
Cd	=	drag coefficient
D	=	specific diameter of the magnetic gliding arc device
d	=	approximate diameter of the arc
d_{corr}	=	corrected diameter of the arc
d_{meas}	=	measured diameter of the arc
E	=	electric field
E_n	=	excitation state energy
F_a	=	ampere force per unit arc length
F_d	=	drag force
f	=	arc rotation frequency
G_0, G_1, G_{ref}	=	identified peaks from an OH spectrum
$I_{nm_{\text{ref}}}$, I_{nm}	=	reference and calculated intensity
I	=	plasma current
i, j	=	indices representing the two nozzle streams
j	=	plasma current density
L	=	distance between counterflow nozzles
Q	=	volumetric flow rate
t	=	exposure time period of high-speed camera
u	=	gas velocity
v_d	=	drift velocity
$Z(T_{\text{ref}})$, $Z(T)$	=	partition functions
ρ	=	gas density

Received 24 April 2006; revision received 30 March 2008; accepted for publication 30 March 2008.

*Professor, Mechanical Engineering and Mechanics Department, Drexel Plasma Institute.
†Research Professor, Mechanical Engineering and Mechanics Department, Drexel Plasma Institute.
‡Graduate Student, Mechanical Engineering and Mechanics Department, Drexel Plasma Institute.
§Associate Professor, Department of Mechanical and Aerospace Engineering.
¶Graduate Student, Department of Mechanical and Aerospace Engineering.

I. Introduction

WITH the ever-increasing want and need for practical high-speed air-breathing propulsion devices comes the major issue of designing a supersonic combustion system. Depending upon the Mach number, the residence times in the combustor of a scramjet may be on the order of the reaction time. This is not as much of an issue for fuels such as hydrogen because of their rapid ignition and reaction times, but it does become a significant issue for hydrocarbon fuels because of their longer ignition delay times. Specifically, the two most critical problems in scramjet development arise in the form of ignition and flame stabilization in the supersonic combustor.

Over the course of the last few decades, much research has been focused on supersonic combustion development and has brought our understanding a long way closer to a tangible and reliable system. Many solutions have been realized in this regard, ranging from passive cavity flame holders [1–5] to energy addition via precombustors [6–8] and plasma [9–17], to combat the aforementioned problems in supersonic flow systems. Cavities or ramped cavities provide a subsonic region for flame stabilization as well as enhanced mixing, but do not add any energy to the system, setting an upper limit on the extent of enhancement. By adding energy to the flow via a precombustor, especially in conjunction with a cavity, the flame becomes more stable with increased flammability limits. Here, the elevated temperatures and radical pools produced during the combustion have proven to be an effective means of decreasing the ignition time and increasing the flame stabilization. Unfortunately, this method is constrained by the requirement of an additional combustion chamber and, more importantly, by the flammability limits of the fuel–air mixture in the precombustor, especially for hydrocarbon fuels. In this regard, plasma-based ignition is a promising technology because it is not constrained as much by the flammability limits of a mixture, as is the case with a precombustor or cavity flame holding design. To address this issue, plasma has been

put forth in many configurations ranging from plasma torches [9,10] to high-voltage nanosecond discharges [11,12].

To determine the best kind of plasma system to be applied to ignition and combustion applications, we need to classify the various possibilities of electrically generated plasma discharge configurations into types that may be effective for the enhancement process. Plasmas are broadly classified into two categories, namely, thermal (or equilibrium) and nonthermal (or nonequilibrium). Thermal plasmas include arc discharges, plasma torches, and radio frequency inductively coupled plasmas. The stepwise processes of ionization and dissociation take place via large amounts of energy or heat addition. Because of this heat addition, the gas temperatures are very high (5000–50,000 K), with electron temperatures of the same order and energy input in all degrees of freedom. Also, it is unnecessary to have such a high increase in gas temperature from the point of view of ignition. This results in poor chemical reaction selectivity of the ignition process. In addition, there would be either large power requirements or localized activation, such as with a plasma jet (e.g., only penetrating into a small portion of a transverse supersonic flow). Furthermore, to scale up a thermal plasma discharge, much higher specific power inputs are required.

Nonequilibrium plasmas have been traditionally generated in low pressures, such as direct-current glow, corona, radio frequency, microwave, and nanosecond high-voltage discharges. Unlike thermal plasmas, they have high chemical selectivity and are capable of homogeneous activation. The primary means of dissociation and ionization is direct electron impact from high-energy (speed) electrons accelerated by a large electric field. However, homogeneous activation leads to power requirements that can become extremely high, sometimes in excess of several MJ/m^3. Also, the gas temperatures typically achieved are either room temperature or too low from an ignition assistance point of view.

Therefore, an ideal plasma discharge should have intermediate temperatures between the temperatures of thermal and nonthermal plasma. The temperatures should be high enough for the ignition of a mixture, have activation benefits of a homogeneous discharge, provide high levels of chemical reaction selectivity, have high electron temperatures, and have high plasma densities with low power requirements [16]. The discharge that aptly suits this description is the gliding arc (GA). The GA is a unique nonthermal plasma that has a relatively high plasma density, power and operating pressure in comparison with other nonequilibrium discharges, a high electron temperature (>1 eV), relatively low gas temperatures (<3000 K), and good chemical selectivity in comparison with thermal discharges. High-temperature electrons are more efficient at producing ions, radicals, and excited and dissociated molecules than those in equilibrium plasma (<1 eV), and the gas temperatures are still high enough to accelerate the interaction between neutral species. Also, the GA is known for its simplicity of design and applicability.

After establishing the GA as best suited for the parameters sought for our system, the next step is to understand under what conditions and to what extent there will be thermal and nonthermal effects. It is very clear and has been shown many times over that radical addition will shorten the ignition time. But what is not yet clear is to what extent the radicals can enhance a system, specifically from the flame stabilization and burning rate perspective. This question of "nonthermal enhancement" has long been debated [9,10]. Furthermore, is it possible to enhance a flame using plasma in a way that can not be explained by traditional combustion chemistry? To even begin to answer these questions, a system has to be developed to provide an ideal or, at a minimum, simplified platform to study the plasma–flame interaction. This can be a daunting task because of the complexity of the interaction between the plasma discharge, flowfield, and flame.

The GA plasma discharge, which has been chosen as the basis of our work, has its roots in a traditional flat gliding arc system, as can be seen in Fig. 1. The arc is initiated at the shortest gap between the two electrodes, after which it elongates by transverse gas flow. Within a short time (microseconds), the arc current reaches its maximum value whereas the voltage drops to almost zero. As the gas flow pushes the arc, its voltage increases and the current starts to decrease. The elongating arc demands more power to sustain itself, until it reaches the maximum that the power supply can provide. However, due to continuous gas flow, the length of the arc continues to grow but the power supplied by the source is insufficient to balance the energy losses to the surrounding gas. If the power supply is capable of providing sufficiently high voltage, the arc changes its ionization mechanism to a nonthermal one, that is, stepwise to direct. Because of instability, the arc cools down and finally extinguishes, marking the end of one cycle. The next cycle of the arc evolution begins as the voltage in the gap reaches its breakdown value and initiates at the shortest gap once again. The transition is attributed to a continuous increase in the electric field until extinction, causing electrons to gain energy during transition, coupled with convective cooling of the gas in the plasma arc. Figure 2 shows the increase in electric field after the point of transition. From the perspective of using plasma for an ignition enhancement study, the traditional flat GAs pose a problem because of the requirement of high-flow rates of transverse gas to obtain more-or-less uniformity of the discharge and also the inability to stabilize the nonthermal portion of the discharge.

The goal of this research was to develop an ideal and simplified GA plasma discharge and to integrate it with a counterflow burner (known for its ease of study) to secure a more fundamental understanding of the interaction between species generated by nonequilibrium plasma and diffusion flames. This was accomplished by first designing a magnetically stabilized nonequilibrium gliding arc plasma (MGA) discharge system. The design, development, and diagnostics of this system are discussed further in this paper. This

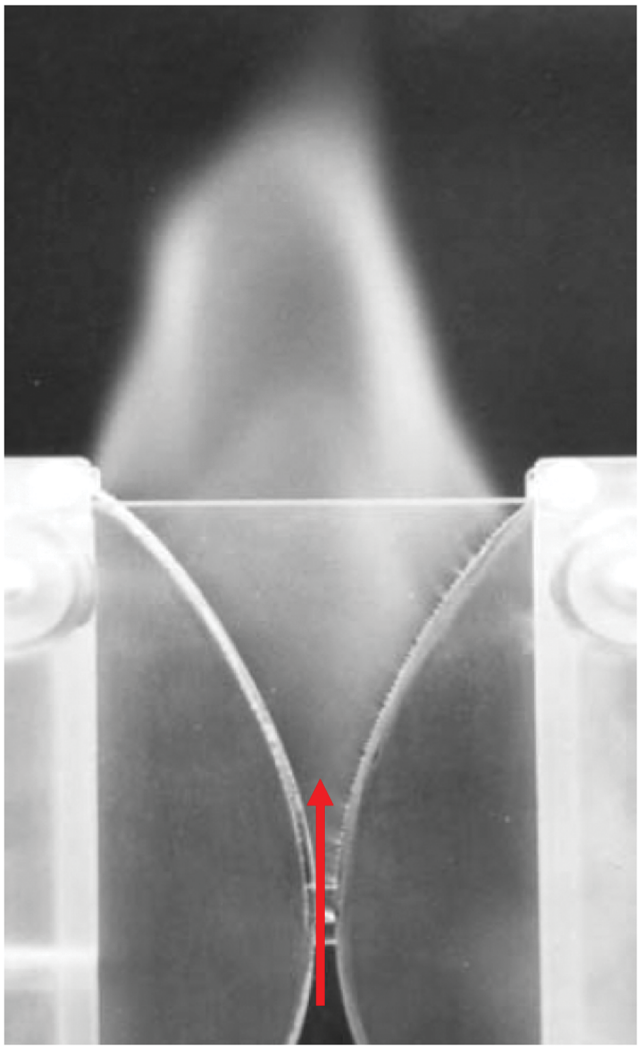

Fig. 1 Traditional flat gliding arc (arrow points in the direction of airflow).

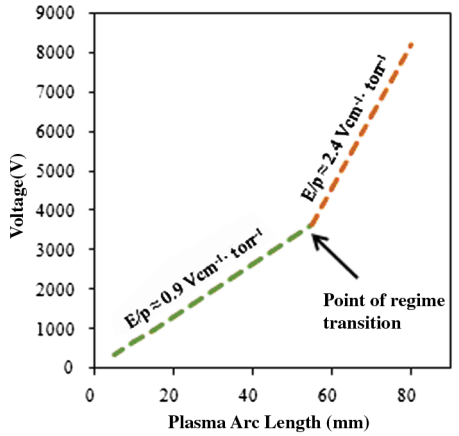

Fig. 2 Increase in the electric field in plasma after the transition point in GA [35].

MGA system was then integrated with a counterflow burner, providing a simple platform to study the plasma–flame interaction. A detailed analysis of the MGA and the flame was performed. This included optical spectroscopy of the MGA and experimental studies of the extinction behavior, laser diagnostics for flame temperatures via planar Rayleigh scattering, and OH number densities via OH planar laser-induced fluorescence (PLIF) for counterflow diffusion flames. These results were then compared with numerical computations using detailed chemistry to validate the measurements and clarify the roles of thermal and nonthermal effects in nonequilibrium-plasma-assisted combustion.

II. Design and Development of Magnetic Gliding Arc

A. Principle

As discussed earlier, one of the key problems with the employment of traditional GAs for purposes of combustion studies is that the nonequilibrium portion of the discharge extinguishes rapidly after transition. However, recently it was found that, during the gliding arc cycle, the arc can be stabilized well past the transition from the thermal equilibrium to the nonequilibrium regime before extinction [17]. This was an extremely important result, as it opened up the possibility of stabilization of a strongly nonequilibrium gliding arc discharge. One of the technical solutions to achieve this was to drive and elongate the arc using a force other than transverse gas flow.

We used the concept of Lorentz force, wherein a moving charge in a magnetic field is subjected to a force. The direction of motion of the charge due to this force is determined by the well-known right-hand rule: if you orient your right-hand palm open, such that the fingers determine the direction of magnetic field and the thumb points toward the direction of motion of the charge, then the palm faces the direction of force experienced. In dc discharges such as the MGA, there is no switching of polarity between electrodes. The directions of motion (between electrodes) of negatively and positively charged species are opposite. However, they experience a force in the same direction due to their charge (transversely). This inherently facilitates the motion of the arc as a single unit. We extend this to the concept of ampere force, wherein the applied magnetic field was normal to the length of the current-carrying "plasma arc conductor," causing it to move. The plasma arc can be stabilized near extinction in the nonequilibrium regime for an indefinite amount of time.

B. Construction

The MGA apparatus, as seen in Fig. 3, is composed of stainless steel inner and outer electrodes, which serve as the cathode (high voltage) and anode (grounded), respectively. A wire is fixed to the cathode that is kept separated from the outer anode by approximately 2 mm at the smallest gap (point 1 in Fig. 4). The spiral wire gets

Fig. 3 Photographs of the magnetic gliding arc device: front, top, and isometric views.

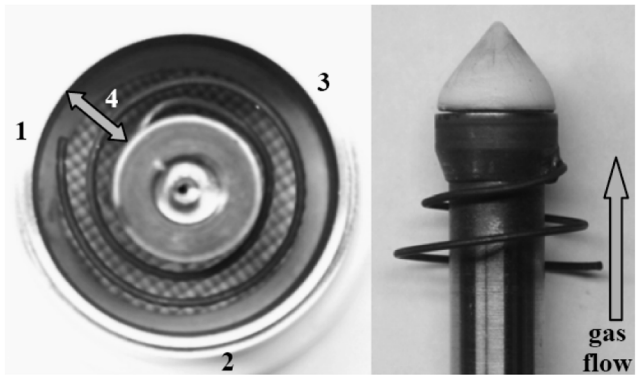

a) b)

Fig. 4 Gliding arc plasma system: a) top view of system, and b) side view of central electrode. Numbers indicate the path of the gliding arc from initiation (1) to arc rotation/elongation (2) and (3), and, finally, to arc stabilization (4).

progressively closer to the cathode (inner electrode) to which it is attached, at the largest gap between the two electrodes. In addition, there is a magnetic field in the discharge region produced by an external donut-shaped permanent ceramic magnet, as seen in Fig. 3 (Adams Magnetic, Inc.). The direction of the magnetic field determines the direction of the rotation of the arc (in this case, counterclockwise to follow the wire when looking down upon the system, as in Fig. 4). The magnetic field strength as well as the plasma current determines the frequency of rotation discussed later in this paper.

C. Magnetic Field Strength

Simulations were performed using finite-element-based software, Ansoft Maxwell SV, to estimate the magnetic field strength in the zone in which the plasma rotates. The 2-D simulation results presented in Fig. 5 show that the magnetic flux lines are parallel to the axis of the reactor (on the inside). Hence, when the arc is initiated along the radial direction, the electric and magnetic fields are normal to each other at all times. Figure 6 displays contours of magnetic field B in tesla in the vicinity of the reactor. Figure 7 shows a plot of variation of the magnetic field as a function of the distance between the electrodes at the plane where the arc stabilizes. Hence, the

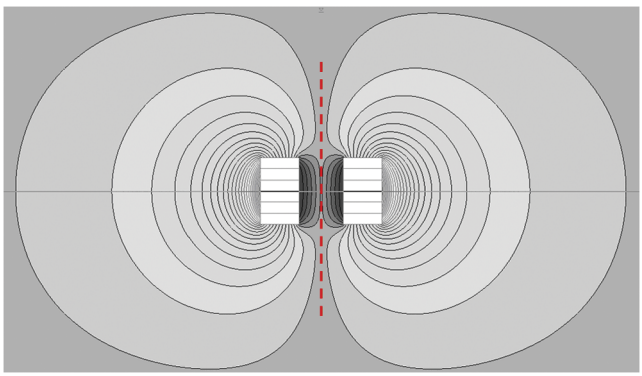

Fig. 5 Magnetic flux lines predicted in 2-D simulation by Ansoft Maxwell SV; it can be observed that the flux lines run parallel to the axis of the reactor (dashed line).

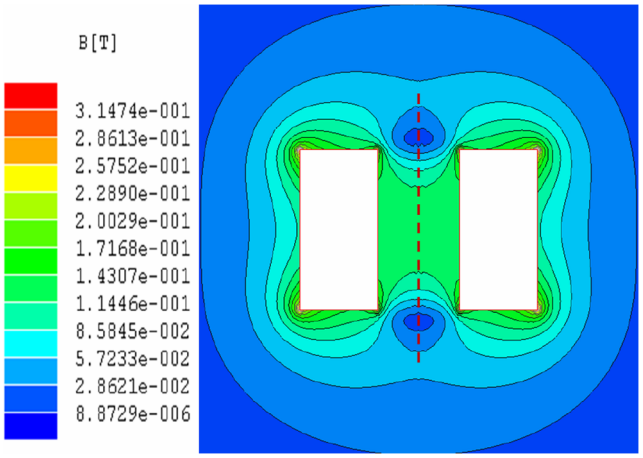

Fig. 6 Contours of the magnetic field distribution in tesla in the vicinity of the MGA device.

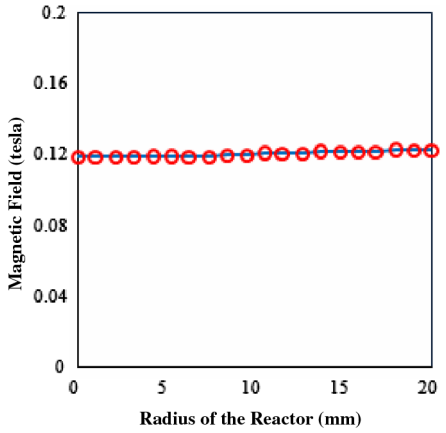

Fig. 7 Magnetic field variation along the radial distance between the inner (cathode) and outer (grounded) electrodes at the plane of rotation of the MGA plasma disk.

average magnetic field in the discharge zone can be approximated to be 0.12 T. This is a reasonable estimate for the magnetic field typically produced by ceramic magnets.

D. Rotating Plasma Disk and Uniformity

When a high-enough voltage is applied to the plasma device, there is an initial breakdown of the gas at the shortest gap between the electrodes, and a quasi-thermal arc plasma is established. The arc then rotates in the magnetic field and elongates as the distance between the spiraled wire and the outer electrode increases (as seen in Fig. 4 from point 1 to 2 to 3). The increased length of the arc results in the transition to a nonequilibrium plasma, leading to more rapid cooling and intermediate temperatures (2000–3000 K) as well as an increase in electric field and average electron temperatures (>1 eV). Once the arc reaches the cylindrical inner electrode (point 4 in Fig. 4), there is a stable rotating intermediate temperature arc in the gas flow. A top view of this plasma disk can be seen in Fig. 8. The plasma arc rotation frequency ranges from approximately 20 to 50 Hz (during a range of operation of a current of 30–90 mA) and only decreases by a few percent when the flow rate is increased (Fig. 9). The increased rotation frequency comes from the higher current input (and hence, higher power addition), forcing the arc to rotate faster in the fixed magnetic field. When the arc reaches the largest gap, it remains at a fixed axial position with a constant length as it rotates. This is because the arc is no longer convecting downstream. The GA sustains itself during this period of continuous rotation between electrodes. This is because it moves repeatedly through a media that was previously ionized. It therefore requires less power input to remain at that position (stabilize) as opposed to quenching and reinitiating at the smallest electrode gap, as it does in the flat geometric configuration. Because the frequency of rotation of the arc is fast when compared with the gas velocity, there is quasi-uniform activation of the flow.

To emphasize this point, a simple model was proposed to estimate the flow rate, Q, of gas that could be quasi-uniformly activated by the gliding arc. The system was designed such that the plasma disk stabilizes at the largest gap between electrodes, that is, 10 mm. The magnetic field strength at this location is 0.12 T (estimated value from simulations). The low-current, high-voltage gliding arc operation would have an electric field strength, E, for the case of the gliding arc propagation through nonionized air of about 0.1 kV/mm. This would lead to a gliding arc voltage drop of 1 kV for the given length of the gap. We make an assumption that the arc is "not transparent" to the surrounding air, that is, it experiences a drag force as it rotates. Hence, the plasma arc behaves like a current-carrying cylinder (wire) that experiences two sets of forces, namely, ampere force per unit length, $F_a = IB$ (assuming the current and magnetic field are normal at all times), and drag force per unit length, $F_d = C_d \rho u^2 d$. Here, C_d is the coefficient of drag, ρ is the density of air ($\sim$1.29 kg/m^3), u is the velocity of propagation of the arc, and d is the approximate diameter of the arc. Under steady-state or equilibrium conditions, we can approximate: $F_a = F_d$. The limits for the drag coefficient for a very wide range of Reynolds numbers (from 10^2 to 10^5) are $1.3 < C_d < 1$ [18].

Let us consider a specific case of 32 mA of operation. We use the aforementioned parameters in the force balance equation proposed earlier. The arc that is stabilized is approximately 0.385 mm in diameter (measured by a high-speed camera for a current of 32 mA) and moves relative to the gas flow at a velocity of approximately 2.44 m/s. Using the mean diameter of the reactor to compute the

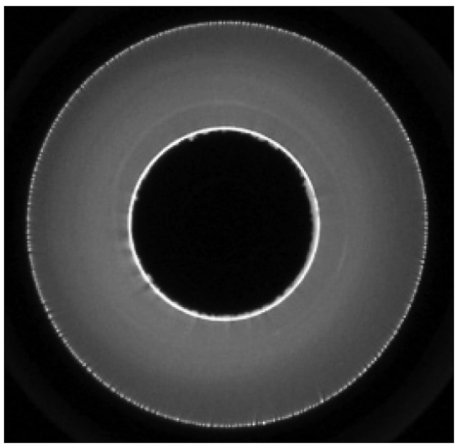

Fig. 8 Top view of MGA plasma disk.

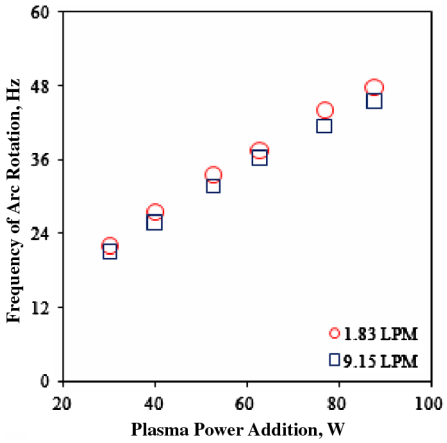

Fig. 9 Frequency of arc rotation for two airflow rates.

circumference covered during one rotation, we can estimate the average rotation frequency of the arc is $\sim u/(\pi D)$, where D is the mean diameter ($\sim$3.2 cm) of the reactor that the arc sees. The corresponding average rotation frequency value is $\sim 2.44/(\pi^{*}0.032) \sim 24$ Hz. This value matches up reasonably well with experimental value reported in Fig. 9 for approximately 37 W ($\sim$32 mA). This means that at a 32 mA current, the arc will appear at the same location 24 times in a second. Hence, the flow will be treated for sure if it passes the diameter of the arc within ($\sim 1/24$ s) 0.041 s, and so the velocity of airflow that will be treated uniformly by the discharge is approximately d/τ, which upon calculation gives us 0.94 cm/s. This corresponds to a flow rate, Q, of 10.7 cm^3/s or 600 standard cm^3/min.

E. Power Supply

The electrical circuit typically used for gliding arc discharges [16] is shown in Fig. 10. As discussed earlier, the quasi-thermal regime exists (due to restriction of current by external resistance) as long as the power supply is capable of providing enough energy to compensate for losses to its surroundings during arc elongation. The transition to nonthermal regime happens at a critical point, when the power drop in plasma is equivalent to that dropped on the external resistance. In order words, this happens when the plasma resistance nearly equals the external resistance [17].

A power supply was custom made (Quinta, Ltd.) to efficiently supply the needs of the gliding arc system stabilized by the magnetic field. It was designed to produce a magnetically stabilized arc with the capability of restricting current while maintaining smooth current regulation. This was accomplished by minimizing the active energy losses with the use of a reactive capacitive resistance that imitates the resistive voltage at all times. To minimize the output electric capacity and to provide the voltage-current characteristic of the power supply (which is close to the resistive voltage-current characteristics), changing the frequency of the high-voltage converter allowed variation of the virtual resistance. After the output rectifier, there was unidirectional voltage and current with a very high frequency of the residual pulsation. The plasma arc behavior was then the same as that for the plasma arc at a constant current and voltage because of the limited time response of the gliding arc. This ensures that it operated more or less in the nonthermal regime. Also, during operation, the current can be reduced manually (causing a corresponding increase in voltage) to lower values than were possible before it extinguishes and restarts again (i.e., instability sets in).

III. Integration of Counterflow Flame Burner

The counterflow flame system was used because it provides four key benefits. These benefits include minimal buoyancy effects because of forced convection, simplified flame geometry, optical access for laser diagnostics, and, finally, the ability to define a flow velocity gradient (strain rate or inverse of residence time) along the centerline near the stagnation plane of the two opposed jets. This

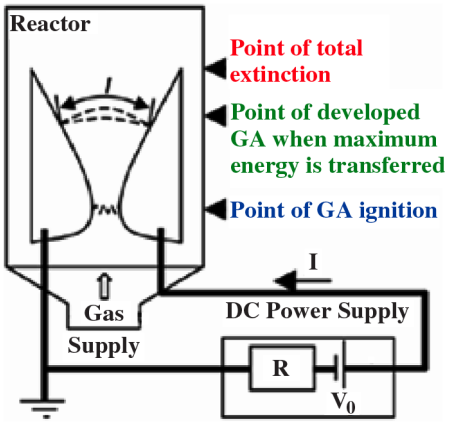

Fig. 10 Schematic of a typical dc gliding arc circuit setup [16].

"global strain rate" can be defined as [19–23]

$$a_i = \left(\frac{2v_i}{L}\right)\left[1 + \left(\frac{v_j}{v_i}\right)\sqrt{\frac{\rho_j}{\rho_i}}\right]$$

Hence, it provides an ideal platform to integrate the MGA with a counterflow flame burner for combustion studies.

A schematic of the system is shown in Fig. 11. It consisted of two converging nozzles of 15 mm in diameter separated by 13 mm. The upper nozzle was water cooled. The gas treated by the MGA was air and exited from the lower nozzle, whereas nitrogen-diluted methane flowed through the upper nozzle. To isolate the flame from the ambient air and disturbances, a nitrogen coflow was used, emanating from a 0.75 mm annular slit around the circumference of each nozzle exit. The velocity of the curtain was maintained at or below the exit speed of the nozzle to minimize diffusion into the stream. The flame was established on the upstream air side of the stagnation plane. The use of this system allowed for examination of the strain rates at extinction.

A DryCal dry piston flow meter (1% error) was used to calibrate sonic nozzles that were employed to control the flow rates of individual gases. The methane and nitrogen were mixed in a hollow mixing cylinder (for minimal back pressure). A bypass system was used to ensure that the mixture input to the flame was held constant while the velocity was increased through the nozzles; hence, the strain increased. The methane/nitrogen mixture, as well as the air, was teed off before the respective nozzles. The flow rate was increased or decreased through the nozzles by closing or opening the valves of the bypasses, respectively. By measuring the flow through the bypass using the DryCal flow meter, the nozzle exit velocities were calculated.

To find the extinction limits, the flame was first established with the bypass fully open and, hence the lowest strained flame. Then each bypass was slowly closed while maintaining the stagnation plane at a fixed position. During this process the flame moved closer to the stagnation plane between the two nozzles, therefore decreasing the residence mixing time as well as increasing the strain rate until flame extinction. Pictures with and without the plasma power addition of the nitrogen-diluted methane–air counterflow flames can be seen in Fig. 12. The one-dimensional structure of the flame can be noted. In all cases the flame was very steady and had minimal curvature, providing an excellent platform to perform experimental measure-

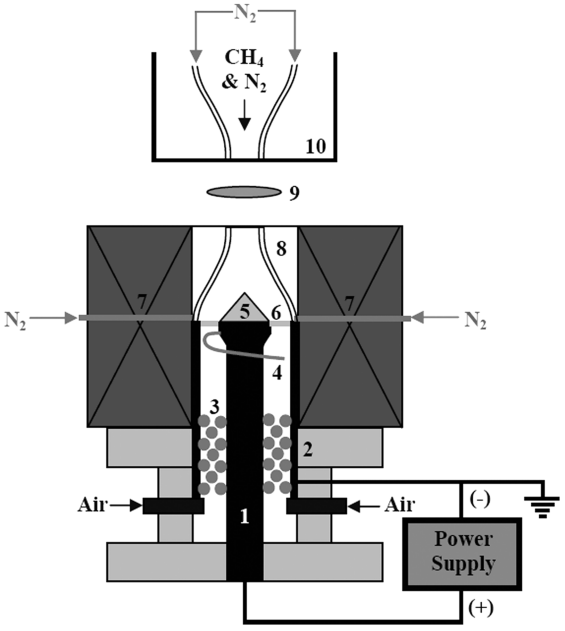

Fig. 11 Counterflow burner with integrated plasma system: 1) cathode, 2) anode, 3) diffuser, 4) gliding arc initiation wire, 5) insulator, 6) plasma disk, 7) magnets, 8) converging nozzle with N_2 curtain, 9) flat diffusion flame, and 10) water-cooled converging nozzle with N_2 curtain.

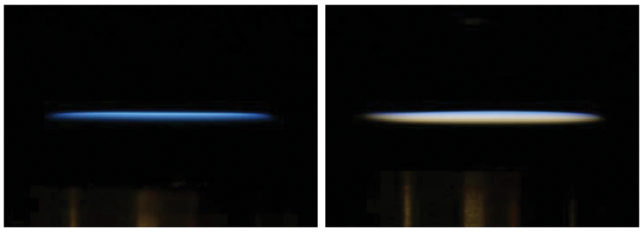

a) b)

Fig. 12 Photographs of methane–air counterflow diffusion flames at a strain rate of 298.5 s^{-1}: a) no plasma power addition, and b) 60 W of plasma power addition.

ments via laser diagnostics. These results were computationally reproducible. There was also a noticeable difference in luminosity between the flame with (Fig. 12a) and without (Fig. 12b) plasma activation of the airstream. The flame with plasma activation of the air had a larger luminous zone with a distinct white and orange coloring as compared with the typical bright blue of the nonactivated flame. This indicated that there was an effect of the MGA on the diffusion flame.

IV. Description of Diagnostic Systems

A. Plasma Diagnostic System

For optical emission spectroscopy from the air plasma, an Acton Research SpectraPro 500i scanning monochromator was used. The entrance slit to the monochromator was placed a few inches away from the discharge, facing the discharge. Spatially averaged emission spectra of the discharge were taken in a range of 200–450 nm. A Roper Scientific model 7430CCD camera was mounted onto the exit slit to digitally acquire the spectra at a resolution of approximately 0.6 nm, with typical acquisition times for the charge-coupled device (CCD) images being 1–5 s. When the discharge was not in operation, a background noise spectrum was obtained. This was then subtracted from the experimental data to improve the accuracy of the results. A low-pressure mercury lamp was used to determine the slit (apparatus) function and calibrate the spectrometer.

For estimations of the current density, an imaging system was used and consisted of a Nikon D70 SLR camera with a Sony CCD-type sensor. The sensor, sized 23.7 mm × 15.5 mm (Nikon DX), was used to capture images at a resolution of 3008 × 2000 pixels (~6 megapixels). The shutter speeds available ranged from 30 to 1/8000 s, which could be used to capture instantaneous arc images. These images were used to determine the approximate widths of the channels at various zones in the plasma discharge.

B. Rayleigh Scattering and OH Planar Laser-Induced Fluorescence for Flame

To obtain a detailed view of the structure of the MGA-activated counterflow diffusion flames, measurements of the temperature profiles and OH distributions were performed via planar Rayleigh scattering and OH PLIF, respectively. A schematic of the systems used can be seen in Fig. 13. A frequency-doubled, injection-seeded Nd:YAG laser (Quanta-Ray GCR-4) with an output of approximately 450 mJ per pulse was used. For OH measurements, the OH was excited via a Lumonics HD-300 dye laser pumped with the aforementioned Nd:YAG laser (Fig. 13). The scattering was imaged with a Princeton Instruments PIMAX intensified CCD camera (one with a photocathode optimized for the visible spectrum for Rayleigh scattering and one for the UV spectrum for OH fluorescence). For Rayleigh scattering, a Nikon 105 mm, f/2.8 macro lens was used whereas, for OH PLIF, a Nikon UV Nikkor 105 mm f/4.5 lens was used along with UG-11 and WG-295 Schott glass filters to isolate fluorescence from the A-X(0,0) and A-X(1,1) bands and block background scattering. Both cameras employed a 512 by 512 pixel array that was binned to improve the framing rate.

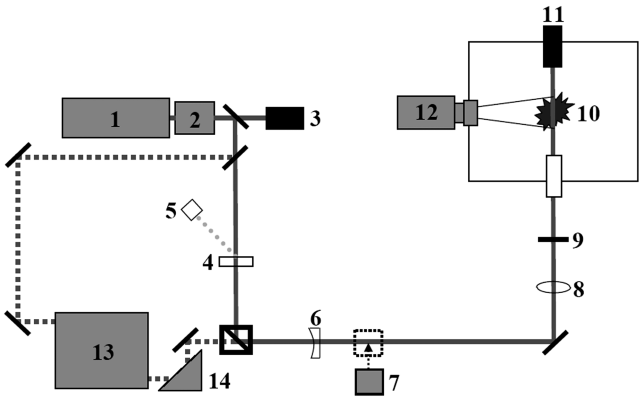

Fig. 13 Planar Rayleigh scattering and OH PLIF setup: 1) injection-seeded Nd:YAG laser, 2) frequency doubler, 3) beam dump, 4) half-wave plate, 5) diode energy meter, 6) lens, 7) power meter, 8) lens, 9) clipper, 10) flame, 11) beam dump, 12) ICCD camera, 13) dye laser with frequency doubler, and 14) Pellin–Broca prism.

To calibrate the Rayleigh scattering signal, images of the scattering intensity were taken of clean, particle-free air (at a known temperature) that was directed through the lower nozzle. To calibrate the intensity seen from the OH PLIF to an absolute number density of OH, measurements were first taken of a known system with the equivalent experimental arrangement. A detailed description of the planar Rayleigh scattering and OH PLIF system operation and calibration has been described in Ombrello et al. [24].

V. Results and Discussion

A. Plasma Characterization

The flat GA has been thoroughly studied over the years for its transition from the thermal to nonthermal regime. However, the MGA is a relatively new discharge that needs to be studied to characterize its nonequilibrium nature. Optical diagnostic techniques were employed to estimate average rotational and vibrational temperatures in the MGA using OH and N_2 emission spectra obtained from the discharge.

1. OH Spectrum for Rotational Temperature

A spatially averaged optical spectrum was obtained from the MGA plasma disk operating at approximately 32 mA, 37 W at normal pressure in air [25]. The experimental spectrum, as seen in Fig. 14, had three major lines, G_0, G_1, and G_{ref}, that were of the most importance in the temperature range from 1000 to 4000 K. This is because the reference peak, G_{ref}, is the strongest group of unresolved lines and G_0 and G_1 are highly sensitive to temperature variation in this range. For temperatures above 4000 K, their sensitivity is

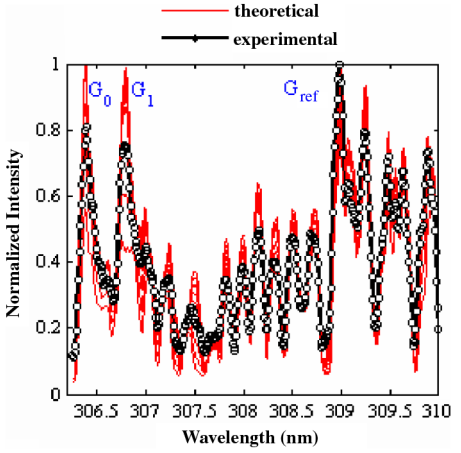

Fig. 14 OH spectrum obtained both experimentally (at ~80 W) and theoretically for different temperatures varying from 1000 to 6000 K.

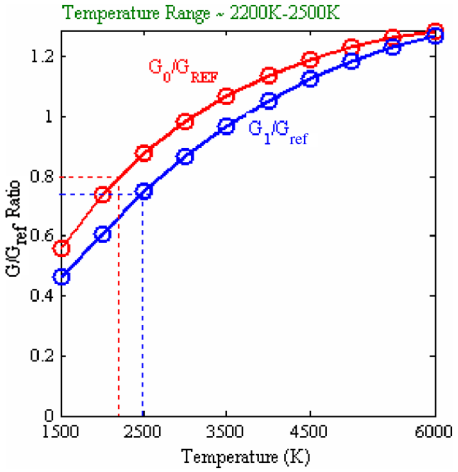

Fig. 15 The ratios of G_0/G_{ref} and G_1/G_{ref} peaks as a function of OH rotational temperature in the MGA. The comparison of the theoretically generated plot with the experimental result yields a temperature of 2350 ± 150 K.

relatively low [26]. Hence, the ratios of these peaks are best considered for diagnostic analysis. A theoretical spectrum was then generated using the technique specified in de Izarra [26] and Pellerin et al. [27] by collecting data pertaining to the OH spectrum as studied by Dieke and Crosswhite [28] in the paper of de Izarra [26], wherein weak transitions were neglected and a set of delta functions corresponding to the strong transitions were generated from the following relation:

$$I_{nm} = I_{nm_{\text{ref}}} \frac{Z(T_{\text{ref}})}{Z(T)} e^{\frac{-E_n*(T_{\text{ref}}-T)}{(T*T_{\text{ref}})}}$$

where I_{nm} is the intensity of the OH transitions (in nanometers) and occurs at a specific wavelength, E_n is the energy of the initial state, and T_{ref} is the temperature at which the reference intensities $I_{nm_{\text{ref}}}$ were obtained. The parameters were taken from the fundamental data found in de Izarra [26]. There, the ratio of the partition functions, $Z(T_{\text{ref}})/Z(T)$, was assumed to be unity. By using different values of temperature, T, the corresponding normalized intensities were computed. Delta functions corresponding to each transition were then convoluted with an apparatus function (i.e., impulse response of the optical device) obtained by employing sharp lines emitted by a low-pressure mercury lamp. Figure 14 shows a theoretical plot for temperatures in 500 K increments for the range of 1000–6000 K and their comparison with those measured in the experiments. The best fit of the ratios of G_0 and G_1 to G_{ref} yielded a rotational temperature of 2350 ± 150 K, as shown in Fig. 15. The rotational temperature results obtained from this theoretical analysis were compared with Spectrum Analyzer software to identify peaks and compute rotational and vibrational temperatures.** The results obtained from Spectrum Analyzer software are more refined when larger numbers of correctly identified lines are used. The results obtained (Fig. 16) agreed with our calculations, giving an average OH rotational temperature of ∼2360 ± 400 K. The vibrational temperature computed (Fig. 17) was found to be ∼3500 ± 600 K.

2. *The N_2 Spectrum for Rotational and Vibrational Temperatures*

A spatially averaged N_2 spectrum was obtained from the MGA plasma disk operating at approximately 37 W at normal pressure in air. Using the SpecAir [29] code, the experimental and theoretical plots were compared and, using best fit analysis, the N_2 rotational temperature obtained was ∼3000 K. This result was in agreement with the investigations pertaining to gliding arcs reported previously [30,31]. Figure 18 shows the fit of theoretical and experimental plots, with the best fit obtained for a vibrational temperature of ∼4000 K.

**Data available online at http://www.physics.muni.cz/~zdenek/span/ [retrieved 3 September 2008].

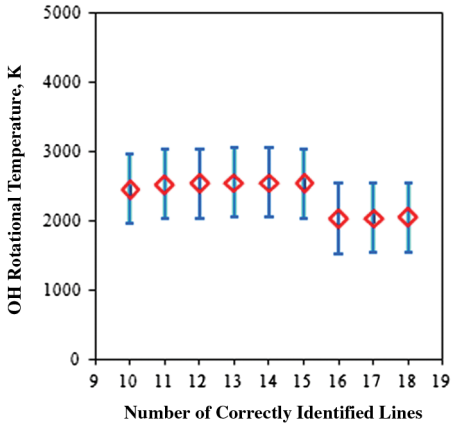

Fig. 16 Spectrum Analyzer OH rotational temperature.

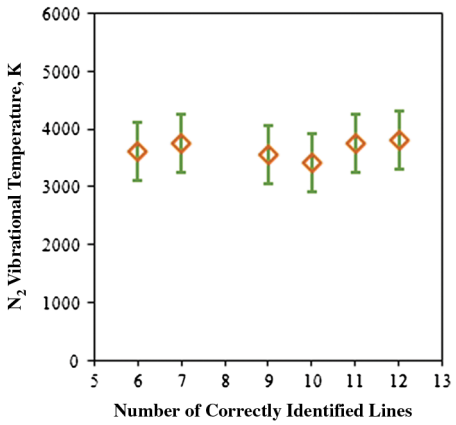

Fig. 17 Spectrum Analyzer N_2 vibrational temperature.

The discrepancy between the spatially averaged temperatures measured using different species (i.e., OH and N_2 in our case) can be specifically explained by the fact that the measurements were conducted without spatial resolution and that the maximum radiation of different radicals could come from different parts of the discharge with different temperatures. For example, in the study of the gliding arc in air using optical methods [32], molecular spectra of OH and N_2^+ band heads at 306.3 and 391.4 nm, respectively, were used. They proposed the plasma column to be divided into two regions, one being the core in which the intensity of N_2^+ lines are observed and the other being the outer "flame" in which the radiation from OH is typical of the surrounding excited molecular region.

A spatially resolved spectrum was also obtained to determine the N_2 rotational temperature in the cathode spot (CS) region (shown in Fig. 19) for 32 mA, 37 W conditions and was found to be ∼1610 K.

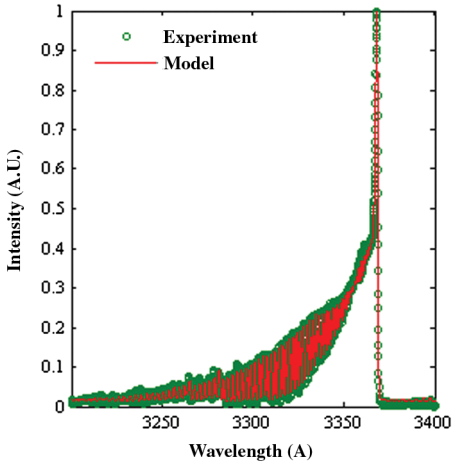

Fig. 18 SpecAir code results for the N_2 spectrum.

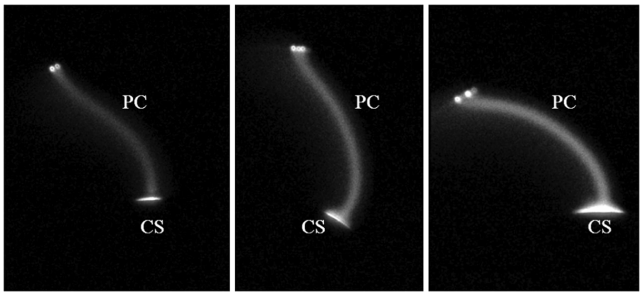

a) b) c)

Fig. 19 Photographs taken by a high-speed camera capturing a single magnetically driven arc in motion. The two main regions of the discharge, namely the CS and PC, can be clearly seen.

A spatially resolved OH spectrum could not be obtained for the present experimental setup because the microscope used restricted our measurements to ~360 nm and above. However, it is within the scope of our future work with the use of UV lenses.

3. *Electric Field in MGA Plasma Arc*

The snapshots in Fig. 19 show the gliding arc structure at different operating conditions: 35 (Fig. 19a), 102 (Fig. 19b), and 158 mA (Fig. 19c). For characterization of the plasma, we split the plasma into two zones, namely, 1) cathode spot or negative glow, and 2) plasma channel or positive column (PC). It was possible to notice that the CS width increased with current, thus keeping the current density nearly constant (covered in Sec. V.A.5 in this paper). This is typical for nonthermal atmospheric pressure glow discharge wherein the normal current density remains constant [33,34]. However, it is important to resolve the electric field in these zones, as it was expected to have a significant voltage drop in the CS.

The typical value for voltage drops in the CS of glow discharges operating in air with iron electrodes is ~260 V [34]. Using visual quantification from high-speed camera arc images, the approximate thickness of the cathode layer (Fig. 19a) is estimated to be ~0.03 cm. Hence, the electric field $E \sim 8000$ V/cm and the reduced electric field $E/n \sim 175$ Td (1 Td $\sim 10^{-17}$ V.cm^2) using a spatially resolved CS temperature of $T \sim 1600$ K.

It follows that the voltage drop in the PC $\sim (1150 - 260$ V$) \sim$ 890 V. Again, imaging analysis yielded a length of the PC to be approximately 1.5 cm. Hence, the electric field $E \sim 593$ V/cm and reduced electric field $E/n \sim 17$–23 Td, using spatially averaged $T \sim 2200$–3000 K.

The electric field can be used as a parameter for the comparison of our discharge with nonthermal glow discharges for which the reduced electric field values typically are in the range of ~3–30 V/cm/torr [34]. Using the calculated effective pressure parameters as discussed, we estimate reduced electric field values of for our conditions of ~6–8 V/cm/torr in the plasma column of the discharge, which is within the range of nonthermal discharges. Also, previous investigations [35] for conventional GA reveal that it is possible to have a nonthermal regime at reduced electric fields as low as 2.4 V/cm/torr.

4. *Average Electron Energy Estimations*

Using the parameters of the system, such as the geometry, and assuming that the electric field is uniform through the PC, the reduced electric field range obtained was for the CS and the PC regions (computed earlier, above). A Boltzmann equation solver, BOLSIG, was employed to calculate the average electron energy vs the reduced electric field for air, that is, 80% N_2 and 20% O_2.[††] The results obtained gave ~4.75 eV for the CS region and ~1.03–1.06 eV for the PC region at atmospheric pressure air conditions. These high electron temperature estimates relative to the rotational gas temperature (energies ~0.13–0.25 eV) suggest the two-temperature (nonequilibrium) nature of the MGA.

5. *Current Density Estimations*

From Fig. 19, it can be noted that there was a change in the width of the plasma column with an increase in current/power on the arc. Considering the arc to have a cylindrical structure, we assume that this width corresponded to the diameter of the gliding arc. By using these diameters and quantifying them based on the length per pixel from known dimensions, we obtain approximate cross-sectional areas of the arc column. In Sec. II.D, the frequency of arc rotation with current was presented. Using these results and the diameters/widths of the arc obtained by visual inspection and quantification at a 1/8000 s exposure time, we needed to incorporate a diametrical correction based on the frequency of arc rotation. These were approximated by the following relation:

$$d = d_{\text{meas}} - \pi D f t$$

where d was the corrected diameter of the arc, d_{meas} was the measured diameter of the arc, D was the diametrical position in the device at which the measurement was taken, f was the frequency of arc rotation, and t was the exposure time. As mentioned earlier, for the nonthermal characterization of plasma, we consider the arc to be divided into CS zone and PC (rest of the arc) zone. Figure 20 shows plasma current density (A/cm^2) results obtained by dividing the value of current with the cross-sectional area, calculated by the aforementioned assumptions. In low-pressure nonthermal plasmas for air at room temperature and iron electrodes, the typical current density is ~300 μA/cm^2/torr^2 [33,34].

In low-pressure nonthermal plasma, the ratio of electric field E to the pressure of operation p, that is, E/p, or the ratio of electric field to the gas number density n, that is, E/n, governs various plasma parameters. It is also sometimes known as the reduced electric field (REF). This scaling is applicable only if the gas temperature is room temperature, which is in the case of low-pressure nonthermal plasmas. However, in the case of atmospheric nonthermal plasmas, the gas temperature is typically higher than room temperature, in which case a scaling needs to be incorporated. The REF parameter is scaled based on effective pressure, $P_{\text{eff}} = P_{\text{atm}}(T_{\text{room}}/T_{\text{actual}})$, where P_{eff} is the effective pressure, P_{atm} is the atmospheric pressure, T_{room} is the room temperature, and T_{actual} is the gas temperature of the plasma under consideration. The scaling is favorably formulated so as to preserve its initial values at room temperature.

Using this result for our conditions, that is, $T \sim 1600$ K (from spatially resolved diagnostic results for the CS zone) and scaling the pressure using the number density, the effective pressure of $P_{\text{eff}} \sim 760$ torr*(300/1600 K) $\sim$ 141.6 torr, and operating at 32 mA, 37 W conditions, we got a current density of ~6 A/cm^2, which is reasonably close to our experimentally estimated value in the CS zone ~4.7 A/cm^2. Also, from spatially averaged rotational

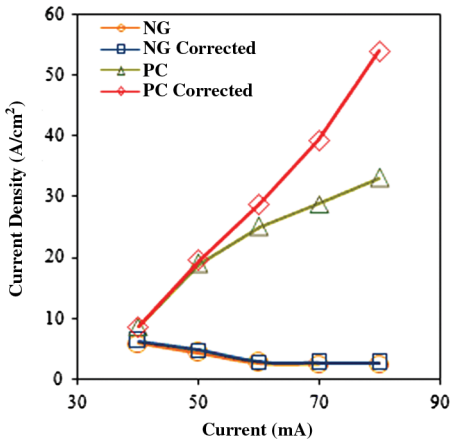

Fig. 20 Estimated MGA plasma current density in the CS and PC.

[††]Data about the Kinema Research & Software BOLSIG, Boltzmann Equation Solver available online www.kinema.com [retrieved 3 September 2008]

temperature values of $T \sim 2200$–3000 K, the current density estimate in the PC zone was ~ 6.9 A/cm^2. As the current was increased, the temperature was expected to increase as well, which decreased the P_{eff} value, thereby decreasing the expected current density from literature estimations. This was observed in the CS data. However, in the PC data, an increase in current density was observed, which possibly could be compared with the property of contraction of nonthermal glow discharge with an increase in current.

6. Electron Density Estimations

The electron density in the PC could approximately be estimated from the current density, j, and the electron drift velocity, v_d, from the relation $j/(e \cdot v_d)$. From the aforementioned estimations, the current density in the PC for $I = 32$ mA is ~ 6.9 A/cm^2. Using $T = 2200$–3000 K, we applied a corresponding $E/n \sim$ 17 Td–23 Td into BOLSIG to compute the electron drift velocity of $\sim(2\text{–}3.7) \times 10^7$ cm/s and thereby the electron density of $\sim(2.2 - 1.2) \times 10^{12}$ 1/cm^3, respectively; this gave an ionization degree of $\sim(6.22 - 4.5) \times 10^{-7}$. These results are reasonably consistent with previous estimations in gliding arcs [30,31].

B. Diagnostics and Measurements of Interaction Between Plasma Species and Diffusion Flame

Experimental measurements of the extinction limits, planar Rayleigh scattering for temperature profiles, OH PLIF for absolute OH number density, and numerical computations with radical addition were performed to quantify the combustion characteristics. Numerical computations were performed using a modified version of the PREMIX code [36] for both potential and plug flow boundary conditions and using the detailed chemical mechanism of GRI-3.0 [37].[‡‡] Temperatures were measured just downstream of the exit of the nozzles via Rayleigh scattering thermometry and were used as inputs into the numerical computation. This was repeated for each of the various flow, concentration, and plasma power conditions.

1. Extinction Measurements

The extinction limits for the counterflow flames were observed with and without plasma power addition. The strain rates for both situations were increased, causing the flame to move toward the stagnation plane, continuously increasing the heat loss and decreasing the residence time for reaction completion, eventually leading to extinction. The measured values for the strain rates at extinction can be seen in Fig. 21 for three different combinations of nitrogen-diluted methane–air counterflow diffusion flames for various levels of plasma power. The extinction limits with no plasma power addition agree well with values reported by Puri and Seshadri [19] and Bundy et al. [23]. It was observed that, by using only 78 W of plasma power input, there was a $\sim$220% increase in the extinction strain rate. This power input was less than 6% of the flame power, defined as the maximum power that could be obtained from the given amount of fuel in the mixture. These results showed that there was a significant extinction limit enhancement by using the MGA activation of the air. However, the reasons for this effect are not apparent as of now.

In the quest to obtain an explanation for the enhancement, the results for the extinction strain rates were then compared with that of the numerical computation. The results shown in Fig. 22 describe the maximum velocities (proportional to the strain rates) achieved before extinction of the flame. Because the input to the computation was only elevated temperatures (obtained from the Rayleigh scattering, to be described in Sec. V.B.2) to mimic the plasma, and both the experiment and computation extinction results were in good agreement, this gave an indication that the effect of the nonequilibrium plasma on the flame was predominately thermal, within the scope of current measurements.

[‡‡]Data available online at http://www.me.berkeley.edu/gri_mech/ [retrieved 3 September 2008].

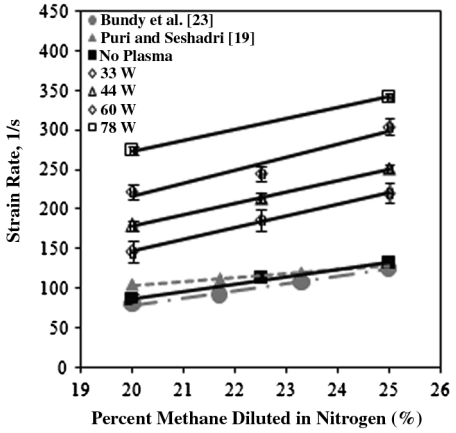

Fig. 21 Effects of plasma power addition on the strain rates at extinction for different levels of nitrogen dilution.

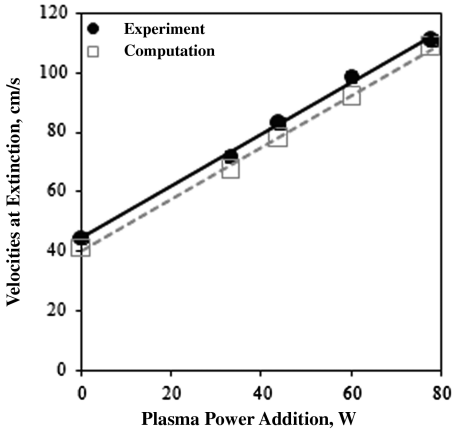

Fig. 22 Comparison of nozzle exit velocities at extinction.

2. Rayleigh Scattering Intensity Ratio and Temperature Profiles

To obtain a detailed look at the structure of the flame enhancement, quantitative measurements of the temperature distribution were found and compared with the numerical simulations. Planar Rayleigh scattering thermometry was performed on the counterflow flame for various strain rates to accomplish this. The laser sheet was passed through the diameter of the disk-shaped counterflow flame between the nozzles of the burner. Two sample images can be seen in Fig. 23, in which Fig. 23a shows no plasma power addition and Fig. 23b shows approximately 33 W of plasma power addition. The background has been subtracted and the air reference divided into each image. The intensity observed was a function of scattering cross sections and number density distributions between the nozzles. The flame was located in the darkest region of these images (transition

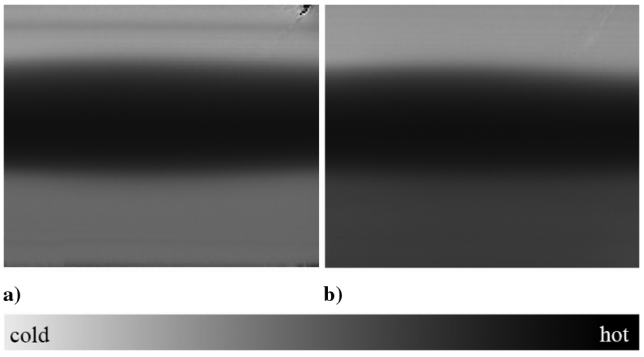

Fig. 23 Rayleigh scattering images at a strain rate of 98.6 s^{-1}: a) no plasma power addition, and b) 33 W of plasma power addition.

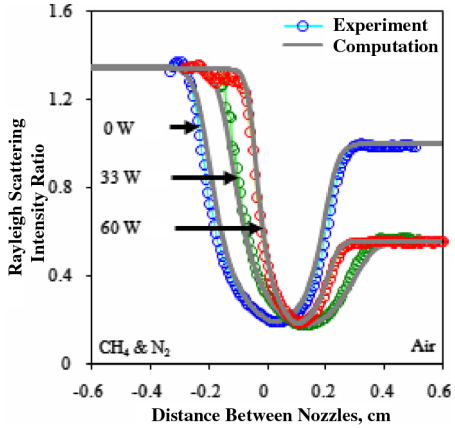

Fig. 24 Comparison of Rayleigh scattering intensity ratio profiles with 0, 30, and 60 W of plasma power addition at strain rates of 87.1, 98.6, and 298.5 s^{-1}, respectively.

from dark to light depicts descending values of temperature and increased scattering). The nitrogen-diluted methane mixture is entering the field of view from the top of the images and the air (MGA side) from the bottom of the images. The one-dimensional flame structure along the flow direction was observed even with the use of the MGA. This result greatly simplified the coupling between the flowfield and the plasma–flame interaction. By comparing the two images, it was possible to differentiate them based on the extent of darkness, indicative of less scattering and higher temperatures. It can be observed that the region below the flame in Fig. 23b (plasma on) is darker than in Fig. 23a (plasma off). In each case, an averaged temperature from a 10-pixel-wide "stripe" was taken from each image. These measured temperatures at the boundaries (just downstream of the nozzles) were then used as boundary conditions in the numerical computation.

The intensity observed by the intensified charge-coupled device (ICCD) camera was a function of both the scattering cross section, because of the distribution of different species, and the number density change between the two nozzles. By simply referencing those intensities to the intensity of air at room temperature, ratios were found. These measurements were then compared with those of the numerical computation, and the results can be seen in Fig. 24 for both the plasma power off (to justify the use of the code for our application) and on. It can be seen that there was reasonably good agreement between the experiment and computation (the oscillations observed can be attributed to the absorptive filters used to "clip" the sheet to reduce scattering off the burner surfaces). Once again, the agreement between the experimental and computational results suggest that the enhancement via the MGA was predominately thermal, within the scope of current measurements.

Because the temperatures, and hence the concentrations of species, change between the nozzles due to the presence of the flame, the scattering cross sections and number densities also change. However, number densities can be estimated from temperature, whereas the scattering cross sections cannot. The scattering cross sections need to be known at each point along the profile as a reference to derive the temperature. Therefore, the species concentrations associated with specific temperatures and axial positions from the numerical computation were used to convert scattering signal to temperature. Using refractory data from Gardiner et al. [38], the variation in scattering cross sections gave accurate temperature profiles from the Rayleigh scattering. The temperature profiles found from the Rayleigh scattering were then compared with the results of the numerical computation at the same input temperatures and flow conditions to further validate the use of the numerical computation for our specific application. Figure 25 shows the temperature profile comparisons of the experimental results via Rayleigh scattering and the numerical computation using the GRI-3.0 mechanism. The profiles, once again, are in good agreement. This further shows that the effect of the MGA on the flame was predominately thermal, within the scope of current measurements.

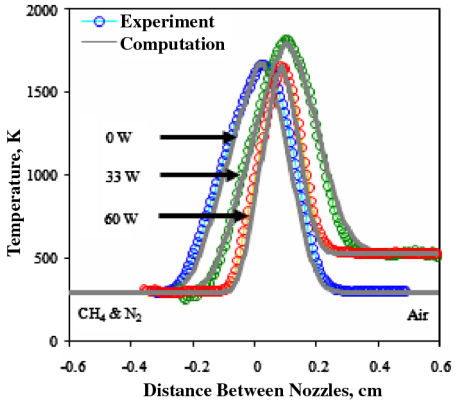

Fig. 25 Comparison of temperature profiles with 0, 33, and 60 W of plasma power addition at strain rates of 87.1, 98.6, and 298.5 s^{-1}, respectively.

3. *OH Planar Laser-Induced Fluorescence Measurements*

To investigate further and confirm that the enhancement of the flame via the MGA was dominated by thermal effects, OH PLIF measurements were performed. The OH number density was measured for different plasma powers and strain rates and referenced to a Hencken burner flame, as described in a previous work by Ombrello et al. [24], to find the absolute OH number density. Figure 26 shows the results from the OH PLIF measurements when compared with the computation with and without plasma power addition. The plots show reasonably good agreement (within the uncertainty range of the measurement $\pm 15\%$) between the experiment and the computation, therefore once again showing that the effect of the MGA on the flame was predominately thermal.

4. *Radical Addition*

Because the enhancement of the strain rates at extinction via the MGA were observed to be predominately thermal, it would be reasonable to calculate the lifetime of the radicals produced by the plasma discharge in the airstream to see if they reach the flame. For this, because the plasma is only activating dry air, it can be assumed that the radicals produced in the flame will only consist of oxygen and nitrogen. As an example, the effect of oxygen atom addition at the air side boundary on the flame structure will be shown (once again mimicking the plasma), because the nitrogen atom addition plays a similar role. Oxygen atom concentrations from 0.01 to 1% were added at the air (plasma) side boundary. The temperature was fixed at 400 K at this boundary to ensure that low-temperature chemistry did not come into play. Also, the velocities at the boundaries were similar to those used in the experiment for a flame that is highly strained and near extinction, for which radical addition may be important. A plot of the temperature profiles and oxygen atom concentration distributions between the nozzles can be seen in Fig. 27. It is shown

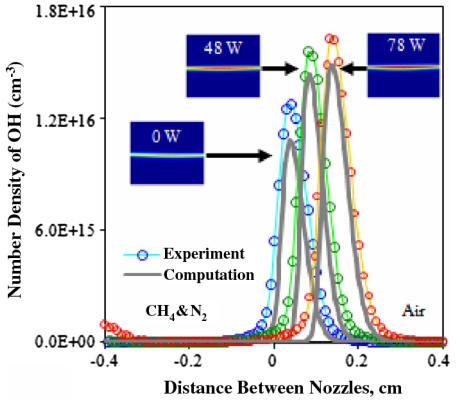

Fig. 26 Comparison of OH number density (cm^{-3}) distributions with 0, 48, and 78 W of plasma power addition at strain rates of 83.3, 127.7, and 183.0 s^{-1}, respectively.

that there was no significant effect until almost 1% oxygen atom addition. The MGA plasma disk is located almost 4 cm upstream of this boundary, which is the production site for oxygen atoms. However, because we do not observe any nonthermal enhancement in our results thus far, it can be construed that these radicals recombine well before they reach the flame, producing only elevated air temperatures. The radical-induced nonthermal effects on the burning rate of diffusion flames are very limited at low air temperatures because the radical lifetime is too short to affect the chain branching reaction path. Figure 28 shows computational simulations of oxygen atom radical lifetimes as a function of temperatures and pressures of operation.

C. Plasma-Induced Ignition Enhancement of Hydrogen

1. *Measurements of Ignition Points for* H_2*–Air Flame*

To observe nonthermal contributions from active species, especially radicals and ions, the previous results suggested that it was necessary for us to go to elevated temperatures or reduced pressures. The first step was to simply consider elevated temperatures. For this, ignition experiments were performed using a preheater and the MGA on the upstream air side of the counterflow burner. This system would allow for increased radical lifetimes, suppressing their rapid rate of recombination. By simply adding a preheater to the current counterflow system upstream of the MGA plasma disk, the apparatus could be transformed into an ignition system that was able to provide elevated temperatures. The combination of the gliding arc, elevated temperatures, and the precondition of no flame, before ignition, would allow for an ideal platform to observe the effect of ignition enhancement. Our experimental data using MGA activation of the airstream, starting with hydrogen as the fuel, could simply be compared with those of the published data on counterflow hydrogen diffusion flame ignition via heated air. Thus, any differences seen between the heated air ignition and the heated air plus gliding arc activation ignition would be nonthermal.

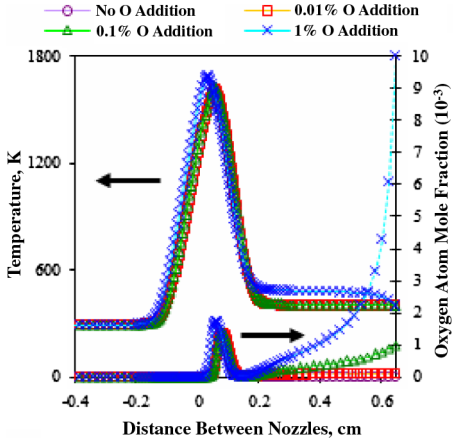

Fig. 27 Computed temperature and oxygen atom distributions between the nozzles of the counterflow system with the oxygen atom addition.

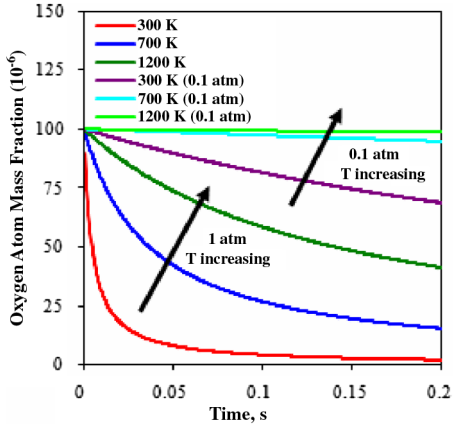

Fig. 28 Oxygen radical lifetimes in air for typical residence times in the MGA counterflow burner system. It is seen that increasing the temperature or reducing the pressure can help the radicals survive until they reach the flame.

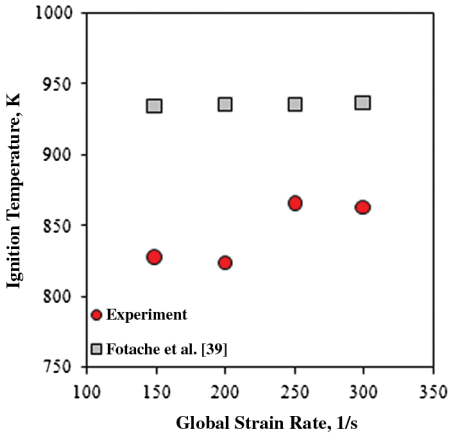

Fig. 29 Comparison of ignition temperatures of counterflow hydrogen diffusion flames using preheater with preheater and gliding arc activation of the airstream.

To accomplish all of this, a silicon carbide heater was placed upstream of the gliding arc plasma discharge device, effectively raising the air temperature to allow for the ignition of hydrogen. The MGA was turned on and the heater power, and hence the air temperature, was raised until the hydrogen diffusion flame ignited. The temperature of the hot airstream was measured with a 0.005-in.-diam type *r* thermocouple axially located between the two jets of the counterflow burner, where the flame would be established. The temperature readings from the thermocouple were corrected for radiation. The results of the ignition temperatures using the preheater and MGA compared with the published data using only a preheater [39] can be seen in Fig. 29. The ignition temperatures obtained are significantly lower than those of just heated air, implying that there is more than just a thermal effect. This can possibly be due to the elevated temperatures leading to longer radical lifetimes. The mechanism of this enhancement needs to be investigated further but, at a minimum, these results offer up the observation of possible nonthermal effects using an ideal system for the plasma–flame interaction.

2. *Autoignition Enhancement of* H_2*–Air Mixtures*

To understand these result better, kinetic computations for the ignition of H_2–air stoichiometric mixtures were conducted using three different mechanisms, namely, Balakrishnan, Matveev and Vlachos, available and simulated in Chemical Workbench.[§§] The ignition time delays for preheated H_2–air mixtures at 900 K were found to be ∼115, 80, and 3 ms, respectively, for the three aforementioned mechanisms. Atomic oxygen radicals (that are expected to be generated from dry air, as discussed earlier) were then added to the incoming charge to observe the radical enhancement effect, if any. When a reduction in delay time was observed for a particular amount of addition of O radicals, the preheat temperature was reduced such that the ignition occurred after the same time delay as it did without radical addition. Hence, it was possible to arrive at a radical concentration that was required to cause the same enhancement effect with the preheat temperature of 800 K. Figure 30 shows that about 0.1–2% by volume atomic oxygen addition is required to cause a 100 K reduction in required preheat. Such a high concentration of radicals is not reasonable even inside nonthermal plasma and especially not after a significant residence time beyond the confines of the plasma.

[§§]Data about Chemical Workbench Software, Kinetic Technologies, KINTECH, Ver. 3.3, available online at www.kintech.ru [retrieved 3 September 2008].

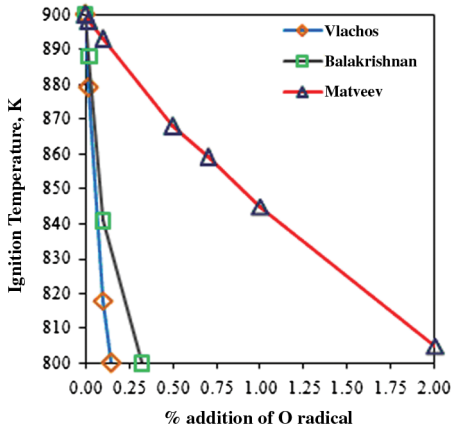

Fig. 30 Comparison of the preheat temperature required to achieve the same ignition delay for various percent volume additions of oxygen radicals using three mechanisms for H_2 air, namely, Balakrishnan, Matveev, and Vlachos.

D. Nonthermal Plasma Ignition and Combustion Enhancement Mechanism

Over the years, researchers have been debating the possible mechanism of nonthermal enhancement of ignition using plasma. For a long time, the radicals produced by plasma were touted to be the contributors to ignition enhancement. From our discussion of radical addition simulations in Sec. V.C.2, it is clear that it is not possible to achieve a significant enhancement effect, as we did in our results presented in Sec. V.C.1, unless we have relatively high concentrations of radicals (∼0.1–2% or more). However, such high concentrations of radicals are not realistic in nonthermal plasma, not to mention the possibility of achieving such concentrations ∼4 cm from the MGA plasma disk, after treatment. Typical time scales before the active species can reach the stagnation zone can be approximated as ∼0.2–0.06 s [40]. This was without considering increased mixing as it passes through the nozzle. This result qualitatively (maybe not quantitatively) proves the intervention of sources other than radicals that contribute to the reduced ignition delay process.

Plasma is a source of active species, meaning it is not only a source of free radicals, but also charged and excited species. The numerical computation used to predict enhancement only accounts for the addition of radicals or an increase in temperature. However, it does not take into consideration the effect of other active species. Ion–molecular reactions are fast processes that typically do not have an activation energy barrier to overcome to initiate a reaction. Hence, they can play a pivotal role in the enhancement process, when ignition is to be achieved in direct contact with plasma. However, in our specific experimental setup, the charged species, just like radicals, are expected to recombine well before they reach the stagnation zone. Some electronically and/or vibrationally excited species, on the other hand, can survive for longer durations of time. However, the time scales at which these processes take place depend upon gas flow rates and reactor geometry. Estimates of typical lifetimes of some metastable species [34] are given in Table 1.

To further bolster this notion of the participation of excited species in ignition enhancement, Anikin et al. [41] recently claimed that the initial stages of hydrocarbon oxidation are determined by their dissociation in collisions with excited oxygen atoms O (^{1}D). Kosarev et al. [42] also demonstrated the reduction in ignition delay by injection of O (^{1}D) into H_2–O_2–N_2O–Ar gas mixtures, wherein it was hypothesized that chain continuation reactions such as $O(^1D) + H_2 \rightarrow H + OH$, $K_r = 2.9 \times 10^{-10}$ cm^3/s, and $O(^1D) + H_2O \rightarrow 2OH$, $K_r = 3.5 \times 10^{-10}$ cm^3/s played a major role in enhancement, whereas $O(^1D) + N_2O \rightarrow N_2 + O_2$, $K_r = 10^{-10}$ cm^3/s, and $O(^1D) + N_2O \rightarrow 2NO$, $K_r = 10^{-10}$ cm^3/s played the role of quenching the excited species. In our system, contributions to enhancement from other excited particles as well are expected, for example, O_2 ($a^1\Delta_g$), which is present in abundance due to the low energy of excitation 0.98 eV and long lifetimes (∼3000 s, see Table 1). Most researchers have not studied its effect as it is difficult to quantify it experimentally. However, theoretical estimations can be made to address the kinetics of excited species [34]. Hence, there is a need to develop a plasma-combustion mechanism that takes into account not only radical and thermal addition effects, but also the interaction between charged, charged–neutral, excited–neutral, and excited–excited species.

Table 1 Typical lifetimes of metastable species [34]

Species	Excitation level	Lifetime, s
N_2	$A^3\Sigma_u^+$	13
N_2	$E^3\Sigma_g^+$	300
O_2	$a^1\Delta_{g+}$	3000
O_2	$b^1\Delta_g$	7

VI. Conclusions

A new type of stabilized gliding arc system, the MGA, was successfully integrated with a counterflow diffusion flame burner to provide an ideal and simplified platform to study the plasma/flame interaction. The well-defined system allowed for detailed experimental and computational studies of the characteristics of the MGA and its effect on the extinction and ignition of counterflow diffusion flames. The results yielded a classification of the MGA as having both thermal and nonthermal properties, proving that it was aptly suited for our system. The MGA was seen to significantly enhance the strain rates at extinction, but the detailed analysis of the flame via planar Rayleigh scattering and OH PLIF, and their comparison with computations using just elevated air temperatures to mimic the plasma, showed that the effect was predominately thermal. These results emphasized the importance of elevated temperatures to extend the radical lifetimes sufficiently enough to reach the flame. The ignition experiments showed that there is a possible nonthermal enhancement, but the exact reasons still remain open to interpretation. Possible explanations have come in the form of active species that cannot be explained by traditional combustion radical chemistry. This offers up the suggestion of a new direction to follow in terms of the quest for the mechanisms of plasma/flame interactions with other active species in plasma such as ions and excited species.

Acknowledgments

This work was graciously supported by the U.S. Air Force Office of Scientific Research under contract number F49620-04-1-0038. Also, we would like to thank Campbell Carter of the U.S. Air Force Research Laboratory for all his diagnostics help and the National Science Foundation under grant CTS-0418403 for the laser diagnostic equipment support.

References

[1] Gruber, M. R., Baurle, R. A., Mathur, T., and Hsu, K.-Y., "Fundamental Studies of Cavity-Based Flameholder Concepts for Supersonic Combustors," *Journal of Propulsion and Power*, Vol. 17, No. 1, Jan.–Feb. 2001, pp. 146–153. doi:10.2514/2.5720

[2] Gruber, M. R., Donbar, J. M., Carter, C. D., and Hsu, K.-Y., "Mixing and Combustion Studies Using Cavity-Based Flameholders in Supersonic Flow," *Journal of Propulsion and Power*, Vol. 20, No. 5, Sept.–Oct. 2004, pp. 769–778. doi:10.2514/1.5360

[3] Yu, K. H., Wilson, K. J., and Schadow, K. C., "Effect of Flame-Holding Cavities on Supersonic Combustion Performance," AIAA Paper 99-2638, 1999.

[4] Yu, G., Li, J. G., Chang, X. Y., Chen, L. H., and Sung, C. J., "Fuel Injection and Flame Stabilization in Liquid-Kerosene-Fueled Supersonic Combustor," *Journal of Propulsion and Power*, Vol. 19, No. 5, Sept.–Oct. 2003, pp. 885–893. doi:10.2514/2.6179

[5] Yu, G., Li, J. G., Zhang, X. Y., Chen, L. H., Han, B., and Sung, C. J., "Experimental Investigation on Flameholding Mechanism and Combustion Performance in Hydrogen-Fueled Supersonic Combustors," *Combustion Science and Technology*, Vol. 174, No. 3, March 2002, pp. 1–27. doi:10.1080/713712992

[6] Guerra, R., Waidmann, W., and Laible, C., "An Experimental Investigation of the Combustion of a Hydrogen Jet Injected Parallel in a Supersonic Air Stream," AIAA Paper 91-5102, Dec. 1991.

[7] Ju, Y., and Niioka, T., "Ignition Simulation of Methane/Hydrogen Mixtures in a Supersonic Mixing Layer," *Combustion and Flame*, Vol. 102, No. 4, Sept. 1995, pp. 462–470. doi:10.1016/0010-2180(95)00047-A

[8] Tabejamaat, S., Ju, Y., and Niioka, T., "Numerical Simulation of Secondary Combustion of Hydrogen Injected from Preburner into Supersonic Airflow," *AIAA Journal*, Vol. 35, No. 9, Sept. 1997, pp. 1441–1447. doi:10.2514/2.266

[9] Takita, K., "Ignition and Flame-Holding by Oxygen, Nitrogen and Argon Plasma Torches in Supersonic Airflow," *Combustion and Flame*, Vol. 128, No. 3, Feb. 2002, pp. 301–313. doi:10.1016/S0010-2180(01)00354-6

[10] Takita, K., Moriwaki, A., Kitagawa, T., and Masuya, G., "Ignition of H2 and CH4 in High Temperature Airflow by Plasma Torch," *Combustion and Flame*, Vol. 132, No. 4, March 2003, pp. 679–689. doi:10.1016/S0010-2180(02)00518-7

[11] Bozhenkov, S. M., Starikovskaia, S. M., and Starikovskii, A. Y., "Nanosecond Gas Discharge Ignition of H2- and CH4 Containing Mixtures," *Combustion and Flame*, Vol. 133, Nos. 1–2, April 2003, pp. 133–146. doi:10.1016/S0010-2180(02)00564-3

[12] Starikovskaia, S. M., Kukaev, E. N., Kuksin, A. Y., Nudnova, M. M., and Starikovskii, A. Y., "Analysis of the Spatial Uniformity of the Combustion of Gaseous Mixture Initiated by Nanosecond Discharge," *Combustion and Flame*, Vol. 139, No. 3, Nov. 2004, pp. 177–187. doi:10.1016/j.combustflame.2004.07.005

[13] Chintala, N., Meyer, R., Hicks, A., Bystricky, B., Rich, J. W., Lempert, W. R., and Adamovich, I. V., "Non-Thermal Ignition of Premixed Hydrocarbon-Air and CO-Air Flows by Non-Equilibrium RF Plasma," AIAA Paper 2004-0835, Jan. 2004.

[14] Sullivan, D., Zaidi, S. H., Macheret, S. O., Ju, Y., and Miles, R. B., "Microwave Techniques for the Combustion Enhancement of Laminar Flames," AIAA Paper 2004-3713, July 2004.

[15] Zaidi, S., Macheret, S., Vasilyak, L., Miles, R., and Ju, Y., "Increased Speed of Premixed Laminar Flames in a Microwave Resonator," AIAA 2004-2721, 2004.

[16] Kalra, C., Gutsol, A., and Fridman, A., "Gliding Arc Discharges as a Source of Intermediate Plasma for Methane Partial Oxidation," *IEEE Transactions on Plasma Science*, Vol. 33, No. 1, Feb. 2005, pp. 32–41. doi:10.1109/TPS.2004.842321

[17] Kuznetsova, I. V., Kalashnikov, A. F., Gutsol, A. F., Fridman, A. A., and Kennedy, L. A., "Effect of 'Overshooting' in the Transitional Regimes of the Low-Current Gliding Arc Discharge," *Journal of Applied Physics*, Vol. 92, No. 8, Oct. 2002, pp. 4231–4237. doi:10.1063/1.1505682

[18] White, F., *Viscous Fluid Flow*, McGraw–Hill, New York, 1974, p. 207.

[19] Puri, I. K., and Seshadri, K., "Extinction of Diffusion Flames Burning Diluted Methane and Diluted Propane in Diluted Air," *Combustion and Flame*, Vol. 65, No. 2, Aug. 1986, pp. 137–150. doi:10.1016/0010-2180(86)90015-5

[20] Maruta, K., Yoshida, M., Guo, H., Ju, Y., and Niioka, T., "Extinction of Low-Stretched Diffusion Flame in Microgravity," *Combustion and Flame*, Vol. 112, Nos. 1–2, Jan. 1998, pp. 181–187. doi:10.1016/S0010-2180(97)81766-X

[21] Seiser, R., Seshadri, K., Piskernik, E., and Linan, A., "Ignition in the Viscous Layer Between Counterflowing Streams: Asymptotic Theory with Comparison to Experiments," *Combustion and Flame*, Vol. 122, No. 3, Aug. 2000, pp. 339–349. doi:10.1016/S0010-2180(00)00139-5

[22] Humer, S., Seiser, R., and Seshadri, K., "Non-Premixed and Premixed Extinction and Autoignition of C2H4, C2H6, C3H6, C3H8," *Proceedings of the Combustion Institute*, Vol. 29, No. 2, 2002, pp. 1597–1604. doi:10.1016/S1540-7489(02)80196-1..

[23] Bundy, M., Hammins, A., and Lee, K. Y., "Suppression Limits of Low Strain Rate Non-Premixed Methane Flames," *Combustion and Flame*, Vol. 133, No. 3, May 2003, pp. 299–310. doi:10.1016/S0010-2180(03)00012-9

[24] Ombrello, T., Qin, X., Ju, Y., Gutsol, A., Fridman, A., and Carter, C., "Combustion Enhancement via Stabilized Piecewise Nonequilibrium Gliding Arc Plasma Discharge," *AIAA Journal*, Vol. 44 No. 1, 2006, pp. 142–150. doi:10.2514/1.17018

[25] Gangoli, S., Gutsol, A., and Fridman, A., "Rotating Non-Equilibrium Gliding Arc (MGA) Plasma Disc for Enhancement in Ignition and Combustion of Hydrocarbon Fuels," *17th International Symposium of Plasma Chemistry*, Aug. 2005, pp. 1042, 1043.

[26] de Izarra, C., "UV OH Spectrum Used as a Molecular Pyrometer," *Journal of Physics D: Applied Physics*, Vol. 33, No. 14, July 2000, pp. 1697–1704. doi:10.1088/0022-3727/33/14/309

[27] Pellerin, S., Cormier, J. M., Richard, F., Musiol, K., and Chapelle, J., "A Spectroscopic Diagnostics Technique Using UV OH Band Spectrum," *Journal of Physics D: Applied Physics*, Vol. 29, No. 3, 1996, pp. 726–739. doi:10.1088/0022-3727/29/3/034

[28] Dieke, G. H., and Crosswhite, H. M., "The Ultraviolet Bands of OH, Fundamental Data," *Journal of Quantitative Spectroscopic Radiation Transfer*, Vol. 2, No. 2, 1962, pp. 97–199. doi:10.1016/0022-4073(62)90061-4

[29] Laux, C. O., Spence, T. G., Kruger, C. H., and Zare, R. N., "Optical Diagnostics of Atmospheric Pressure Air Plasmas," *Plasma Sources Science and Technology* , Vol. 12, May 2003, pp. 125–138. doi:10.1088/0963-0252/12/2/301

[30] Ozlem, M. Y., Saveliev, A. V., Porshnev, P. I., Fridman, A., and Kennedy, L. A., "Non-Equilibrium Effects in Gilding Arc Discharge," *2nd International Symposium on Heat & Mass Transfer*, 1999.

[31] Fridman, A., Nester, S., Kennedy, L. A., Saveliev, A., and Mutaf-Yardimci, O. M., "Gliding Arc Gas Discharge," *Progress in Energy and Combustion Science*, Vol. 25, No. 2, April 1998, pp. 211–231. doi:10.1016/S0360-1285(98)00021-5

[32] Richard, F., Cormier, J., Pellerin, S., and Chapelle, J., "Physical Study of a Gliding Arc Discharge," *Journal of Applied Physics*, Vol. 79, March 1996, pp. 2245–2250. doi:10.1063/1.361188

[33] Staack, D., Farouk, B., Gutsol, A., and Fridman, A., "Characterization of a DC Atmospheric Pressure Normal Glow Discharge," *Plasma Sources Science and Technology* , Vol. 14, No. 4, Nov. 2005, pp. 700–711. doi:10.1088/0963-0252/14/4/009

[34] Fridman, A., and Kennedy, L. A., *Plasma Physics and Engineering*, Taylor and Francis, Philadelphia, PA/London, 2004.

[35] Yardimci, O. M., Saveliev, A. V., Porshnev, P. I., Fridman, A. A., and Kennedy, L. A., "Non-Equilibrium Effects in Gliding Arc Discharges," *Annals of the New York Academy of Sciences*, Vol. 891, edited by P. Fauchais, J. van der Mullen, and J. Heberlein, 1999, pp. 304–308.doi: 10.1111/j.1749-6632.1999.tb08777.x

[36] Ju, Y., Guo, H., Maruta, K., and Liu, F., "On the Extinction Limit and Flammability Limit of Non-Adiabatic Stretched Methane-Air Premixed Flames," *Journal of Fluid Mechanics*, Vol. 342, 1997, pp. 315–334. doi:10.1017/S0022112097005636

[37] Frenklach, M., Bowman, T., Smith, G., and Gardiner, B., "GRI-Mech Homepage," Gas Research Institute, Chicago, 1994.

[38] Gardiner, W. C., Jr., Hidaka, Y., and Tanzawa, T., "Refractivity of Combustion Gases," *Combustion and Flame*, Vol. 40, Feb. 1981, pp. 213–219. doi:10.1016/0010-2180(81)90124-3

[39] Fotache, C. G., Kreutz, T. G., Zhu, D. L., and Law, C. K., "An Experimental Study of Ignition in Nonpremixed Counterflowing Hydrogen Versus Heated Air," *Combustion Science and Technology*, Vol. 109, No. 1–6, Nov. 1995, pp. 373–393. doi:10.1080/00102209508951910

[40] Ombrello, T., Qin, X., Ju, Y., Gangoli, S., Gutsol, A., and Fridman, A., "Non-Equilibrium Plasma Discharge: Characterization and Effect on Ignition," AIAA Paper 2006-1214, Jan. 2006.

[41] Anikin, N. B., Starikovskaia, S. M., and Starikovskii, A. Y., "Oxidation of C1-C10 Hydrocarbons in Stoichiometric and Lean Mixtures with Air and Oxygen Under the Action of Nanosecond Discharge," *43rd AIAA Aerospace Sciences Meeting and Exhibit*, AIAA Paper 2005-0601, Jan. 2005.

[42] Kosarev, I. N., Kukaev, E. N., Starikovskaia, S. M., and Starikovskii, A. Yu., "Comparison of the Efficiency of Nanosecond Gas Discharge and Laser Flash-Photolysis in Initiation of Combustion," *17th International Symposium on Plasma Chemistry*, Aug. 2005, ISPC_sstar.pdf

S. Macheret
Associate Editor